Role of bottom water transport and diapycnic mixing in determining the radiocarbon distribution in the Pacific

Vassil Roussenov and Richard G. Williams
Department of Earth and Ocean Sciences, University of Liverpool, Liverpool, UK

Michael J. Follows
Program in Atmospheres, Oceans and Climate, Department of Earth, Atmosphere and Planetary Sciences, Massachusetts Institute of Technology, Cambridge, Massachusetts, USA

Robert M. Key
Atmospheric and Oceanic Sciences Program, Princeton University, Princeton, New Jersey, USA

Received 31 October 2003; revised 6 April 2004; accepted 22 April 2004; published 12 June 2004.

[1] The mechanisms controlling the distribution of radiocarbon over the deep Pacific are examined using, firstly, a simplified one-and-a-half-layer model and, secondly, an isopycnic circulation model with parameterized radiocarbon sources and sinks. Two mechanisms control the radiocarbon at depth: relatively fast, lateral transport of bottom waters determining the horizontal distribution and a slower balance between advection-diffusion and radio decay in the vertical. In the isopycnic model, there is a strong topographic control of the bottom water spreading, which is more complex than in the idealized model. Sensitivity studies reveal that altering the bottom intensified diapycnic mixing leads to significant changes in the radiocarbon distribution through both the direct diapycnic transfer and, indirectly, by modifying the bottom water transport and northward penetration of young radiocarbon waters. *INDEX TERMS:* 4255 Oceanography: General: Numerical modeling; 4532 Oceanography: Physical: General circulation; 4860 Oceanography: Biological and Chemical: Radioactivity and radioisotopes; 9355 Information Related to Geographic Region: Pacific Ocean; *KEYWORDS:* deep circulation, radiocarbon modeling, Pacific Ocean

Citation: Roussenov, V., R. G. Williams, M. J. Follows, and R. M. Key (2004), Role of bottom water transport and diapycnic mixing in determining the radiocarbon distribution in the Pacific, *J. Geophys. Res.*, *109*, C06015, doi:10.1029/2003JC002188.

1. Introduction

[2] The deep Pacific ocean is a significant reservoir of carbon, the magnitude of which depends on the resident water masses, their rates of ventilation and the relative rate of regeneration of biogenic carbon. Changes in these physical properties and this large carbon reservoir could exert a significant control on the atmosphere-ocean partitioning of carbon. The ability of ocean models to simulate the deep carbon distribution has often been assessed by examining the accompanying radiocarbon distribution. Radiocarbon with a half-life of 5730 years can reveal aspects of the deep, large-scale circulation where, perhaps, a steady state may be assumed. The GEOSECS surveys in the 1970's provided the first view of the global distribution of radiocarbon in the oceans [e.g., *Ostlund and Stuiver*, 1980], which have been significantly augmented by the WOCE survey in the past decade [*Key*, 1996; *Stuiver et al.*, 1996; *Key et al.*, 1996, 2002] revealing in more detail the interbasin gradients and patterns. However, in surface waters and the thermocline, the situation is complicated by the transient signature of bomb radiocarbon entering the ocean from the atmosphere.

0148-0227/04/2003JC002188$09.00

[3] In this study we examine the mechanisms which control the distribution of radiocarbon in the deep waters of the Pacific basin. By comparing modeled and observed radiocarbon distributions we examine the deep circulation of the basin and mechanisms of ventilation. We compare the distributions of radiocarbon with a complementary dynamical tracer, the large-scale potential vorticity. Potential vorticity is dynamically active and its distribution has been interpreted in terms of ventilation and eddy stirring processes for both the upper ocean [*McDowell et al.*, 1982; *Keffer*, 1985] and deep ocean [*O'Dwyer and Williams*, 1997; *Roussenov et al.*, 2002].

[4] We examine the sensitivity of the radiocarbon distributions to enhanced bottom mixing using, firstly, an idealized one-and-a-half-layer model [*Speer and McCartney*, 1992] and, secondly, an isopycnic ocean general circulation and tracer model. The isopycnic framework allows precise control on the mixing rates which are central to this study. Diapycnic mixing impacts the radiocarbon distribution both through a direct transport and indirectly through its control on the large-scale overturning circulation. The weak stratification resulting from the enhanced bottom mixing might in reality be a consequence of enhanced mixing over rough topography [*Polzin et al.*, 1997] or the action of weak geothermal heating possibly important in the North Pacific

[*Joyce et al.*, 1986; *Talley and Joyce*, 1992; *Thompson and Johnson*, 1996].

[5] Classically, the horizontal circulation in the deep Pacific is expected to be cyclonic for a flat-bottomed basin [*Stommel and Arons*, 1960]. However, with sloping sidewalls, an anticyclonic circulation can arise due to the horizontal divergence of fluid upwelling over a dome-shaped basin, called the "hypsometric effect" [*Rhines and MacCready*, 1989]; this response was obtained by *Ishizaki* [1994] for a model study of the deep Pacific. However, the complex bathymetry of the deep oceans can prevent these idealized signatures from dominating the modeled circulation [*Roussenov et al.*, 2002].

[6] In terms of previous model studies of the radiocarbon distribution, *Fiadeiro* [1982] employed an idealized numerical model of the Pacific basin flow and $\Delta^{14}C$ distribution based on the Stommel-Arons view of the deep circulation. The assumption of uniform upwelling led to the "oldest" (lowest $\Delta^{14}C$) waters being incorrectly placed on the bottom. The modeled radiocarbon distribution only compared favorably with the observations when the basin wide upwelling was chosen to be a maximum between the Bottom Waters and Deep Waters.

[7] *Toggweiler et al.* [1989] examined simulations of the prebomb ocean distribution of radiocarbon using coarse-resolution configurations of the GFDL ocean circulation model in the light of the GEOSECS data. The radiocarbon simulations demonstrate that a fully prognostic model better captures the observed tracer distribution than "robust diagnostic" models where temperature and salinity are restored toward observations in the models interior. In the robust diagnostic models the "oldest" Pacific waters are again incorrectly placed at the ocean floor, since incorporating artificial interior buoyancy sources and sinks by restoring to temperature and salinity actually weakens the ventilation of the deep Pacific basin.

[8] Recently, as part of the OCMIP (Ocean Carbon-cycle Model Intercomparison Project) study [*Orr*, 2002], there has been a comparison of coarse-resolution model simulations of the global radiocarbon distribution. The models all show a radiocarbon gradient in the Pacific deep waters with "older" (more negative $\Delta^{14}C$) waters in the northern basin. However, there is considerable variability in basin mean $\Delta^{14}C$ and the interbasin contrasts due to the different model configurations, physical boundary conditions and subgrid-scale mixing coefficients. The sensitivity of the modeled radiocarbon distribution to each of these factors is not yet clear. In this study we examine how the radiocarbon distribution over the deep Pacific is controlled by the circulation and diapycnic mixing using an isopycnal model. Diapycnic mixing rates are most easily and precisely controlled in this framework and realistic topographic variations can be incorporated.

[9] The observed distribution of radiocarbon and PV in the deep Pacific are described in section 2. An idealized one-and-a-half-layer model for the bottom water is applied to understand the radiocarbon distribution in section 3. A more realistic isopycnic model and physical circulation is developed in section 4, extending a previous modeling study for the deep Pacific by *Roussenov et al.* [2002]. The modeled radiocarbon and PV distributions are described in section 5. The sensitivity of the model solutions to changes in bottom mixing is explored in section 6, and the implications of the study are discussed in section 7.

2. Observed Distributions of Radiocarbon and PV

[10] Tracer distributions in the deep Pacific are strongly controlled by the overturning circulation, which is characterized by a northward influx of bottom water, converted to lighter water and returned southward at middepth. This transformation of bottom to deep waters is implicit in the northward deepening and eventual grounding of the denser σ_4 surfaces over the deep Pacific (Figure 1a).

2.1. Radiocarbon

[11] The first basin wide view of the distribution of radiocarbon in the deep Pacific came from the observations of the GEOSECS program in the 1970s, which were presented and interpreted by *Ostlund and Stuiver* [1980] and *Broecker et al.* [1985, 1995]. In the upper ocean, the observed distribution incorporates both natural (preanthropogenic, prebomb) and bomb-produced contributions, while in the deep, older waters it is generally assumed that the data reflect the "steady" preindustrial distribution. A more detailed view of the radiocarbon distribution is now available through the observations from the World Ocean Circulation Experiment (WOCE) [*Key*, 1996; *Key et al.*, 1996; *Stuiver et al.*, 1996; *Key et al.*, 2002].

[12] The radiocarbon distribution in the Pacific reflects the competition between the surface input and the influx in the deep waters from the Southern Ocean, the transport and the systematic decay of the tracer. A meridional section of $\Delta^{14}C$ along 170°W from an optimal interpolation of the WOCE data set (R. M. Key et al., A global ocean carbon climatology: Results from the Global Ocean Data Analysis Project, submitted to *Global Biogeochemical Cycles*, 2004, hereinafter referred to as Key et al., submitted manuscript, 2004) reveals high concentrations in the surface ocean, $\Delta^{14}C > 50$, partly reflecting the bomb source, and maximum concentrations in the upper ocean of the subtropical gyres at 35°N and 40°S (Figure 1b). These high concentrations in the upper thermocline probably reflect ventilation from the subduction of mode waters. At depth, there is a northward transport of dense water, Lower Circumpolar Deep Water (LCDW), into the basin, $\Delta^{14}C \sim -160‰$, from the southern boundary. Decay of radiocarbon leads to decreasing values toward the north and toward middepths as the water mass ages. There is a progressive northward decrease in $\Delta^{14}C$ from $-150‰$ at 60°S to a minimum of $\Delta^{14}C \sim -240‰$ in the middepths at 50°N with a northward spreading plume along the western boundary (Figures 2a and 2b).

2.2. Potential Vorticity

[13] To complement the radiocarbon distribution, we consider the distribution of the dynamic tracer, potential vorticity (PV) defined on the large scale as

$$\mathrm{PV} = -\frac{f}{\bar{\rho}}\frac{\partial \sigma_4}{\partial z}, \tag{1}$$

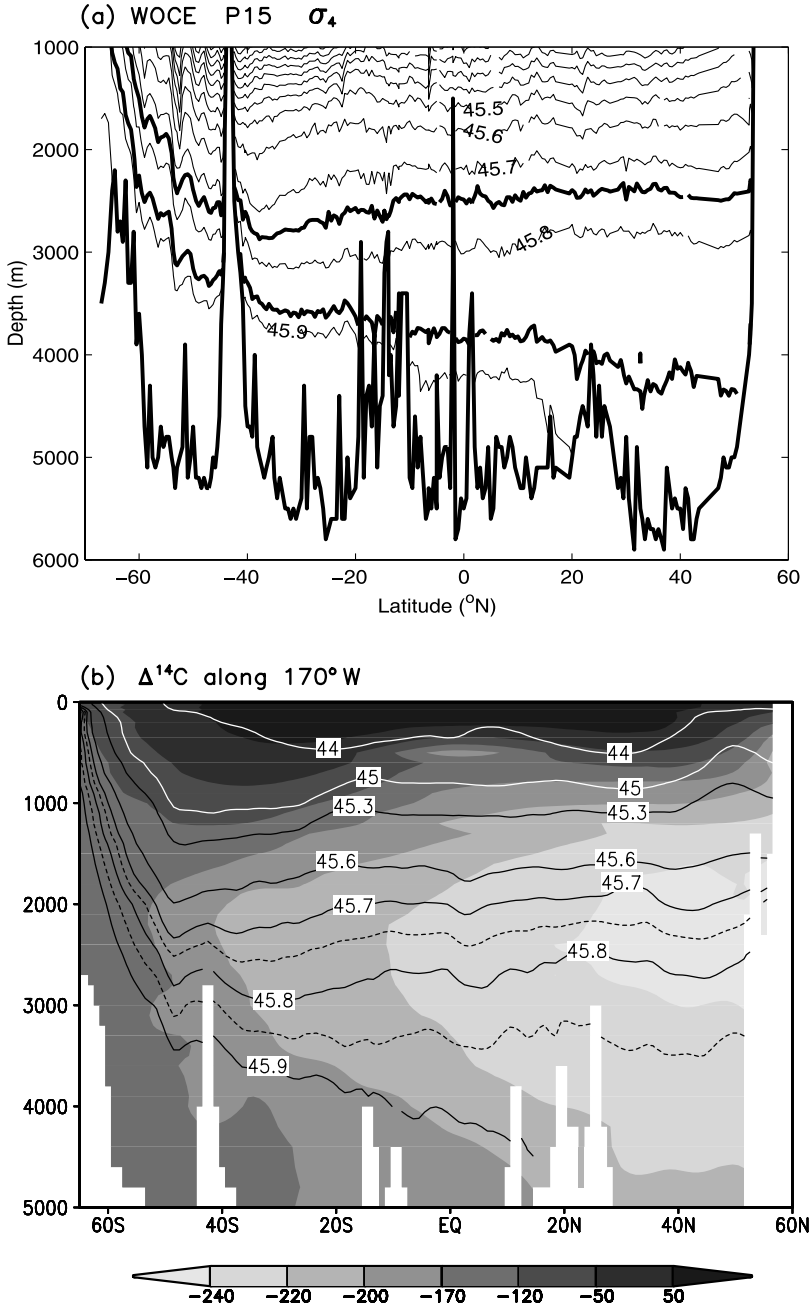

Figure 1. (a) A meridional density section along 170°W in the Pacific (WOCE section P15) for potential density, σ_4, (displayed from 1 km to the seafloor with σ_4 = 45.75 and 45.87 surfaces in bold); (b) meridional section for $\Delta^{14}C$ (shaded) from gridded data along 170°W with isopycnic depths (contours) evaluated from climatology (displayed from the surface to 5 km).

where f is the planetary vorticity, σ_4 is the potential density referenced to 4 km, and $\overline{\rho}$ is a reference density.

[14] For the deep waters, the PV might be expected to increase poleward, reflecting the change in f, assuming that there are only slight changes in layer thickness. However, from the density section in Figure 1a, there are significant changes in stratification and a general northward increase in layer thickness over the deep waters for the North Pacific. Consequently, maps of the PV for deep waters reveal a complex structure, rather than PV contours simply following latitude circles (Figures 2c and 2d) [*O'Dwyer and Williams*, 1997]. There is a northward decrease in the magnitude of the PV from the South Pacific, $>20 \times 10^{-12}m^{-1}s^{-1}$ at 60°S to 0 at the equator, while over the North Pacific, the PV increases northward to $10 \times 10^{-12}m^{-1}s^{-1}$ along the σ_4 = 45.75 surface, but only to $2 \times 10^{-12}m^{-1}s^{-1}$ along the denser σ_4 = 45.87 surface. Hence both the radiocarbon and PV distributions show much larger horizontal differences along the σ_4 = 45.75 surface and weaker contrasts along the denser σ_4 = 45.87 surface. In addition, over the western side of the South Pacific, both the radiocarbon and PV distributions show

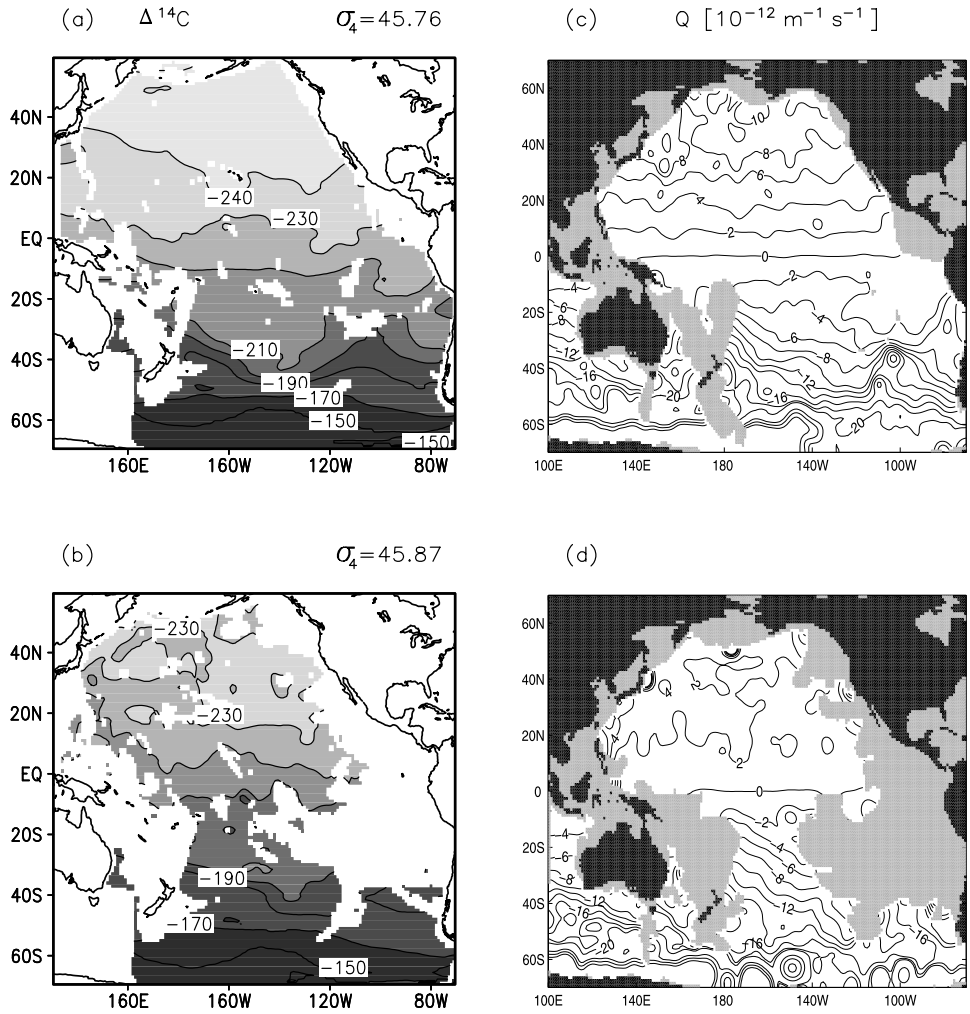

Figure 2. $\Delta^{14}C$ data (‰) mapped on (a) σ_4 = 45.75 and (b) 45.87 surfaces. PV data (10^{-12} m^{-1} s^{-1}) mapped on (c) σ_4 = 45.75 and (d) 45.87 surfaces. The PV surfaces are from *O'Dwyer and Williams* [1997] and are evaluated from NODC data.

signals reflecting the northward transport from the Southern Ocean (Figure 2).

[15] In addition, these maps of PV can be compared with the isopycnal maps of salinity, oxygen and silica on the σ_3 = 41.44 and σ_4 = 45.87 surfaces, and geostrophic flow at the depths between 2500 m and 5000 m calculated by *Reid* [1997]. The PV distributions broadly resemble those of salinity, a conservative tracer. North of the equator, both salinity and PV have stronger meridional gradients on the lighter surface, while oxygen and silica have significant gradients over the denser surface for the North Pacific reflecting their nonconservation. *Reid* [1997] argued that the wind forcing influences the circulation over the water column for much of the North Pacific: flow is dominated by large anticyclonic gyres at mid latitudes in each hemisphere, contracting poleward at depth. In the deep and bottom water, a western boundary current transports high oxygen and low salinity from the Southern Ocean at least as far as the mid latitudes in the North Pacific, while in the eastern interior, lower oxygen and higher silicate concentrations suggest a southward return flow from the Northeast Pacific.

[16] We subsequently investigate how the radiocarbon distributions are controlled by the circulation using, firstly, a simplified one-and-a-half-layer model together with vertical diffusion and, secondly, with an isopycnic general circulation model and examine the connection with the modeled PV distribution.

3. Idealized Model of the Bottom Water

[17] As a starting point, we assume that there are two regimes, horizontal and vertical with different controlling processes, determining the radiocarbon distribution. Firstly, a relatively rapid tracer transport in the bottom water on a timescale of 100 years. Secondly, a much slower, vertical balance involving vertical advection, diffusion and tracer decay on a timescale of several 1000 years. Accordingly, we construct a simplified model to represent these two balances and explore how the strength of diapycnic mixing affects each of them.

3.1. One-and-a-Half-Layer Model for an Idealized Northern Basin

[18] In order to understand the relationship between diapycnic mixing and the transport of bottom waters at a steady state, we consider an idealized one-and-a-half-layer

model for the bottom waters in a northern basin following *Speer and McCartney* [1992]. The model assumes there is a single moving layer of bottom water, which is overlain by a thick, motionless ocean. At a steady state, the vertical velocity at the interface is assumed to be entirely diapycnal. The model assumes that the basin is flat and square with a zonal width and north-south extent of L extending from the equator into the northern basin to 50°N. If the interface between the bottom moving layer and stagnant ocean is given by a height h above the seafloor, then the geostrophic velocities in the bottom layer are given by

$$fv = g' \frac{\partial h}{\partial x} \tag{2}$$

$$fu = -g' \frac{\partial h}{\partial y}, \tag{3}$$

where f is the Coriolis parameter and g' is the reduced gravity based on the density contrast between the bottom layer and the overlying ocean. The meridional transport in the bottom layer is given from linear vorticity balance by

$$\beta v h = f w, \tag{4}$$

which, combining with equation (2), gives

$$\frac{\partial h^2}{\partial x} = \frac{2f^2 w}{\beta g'}, \tag{5}$$

where $\beta \equiv df/dy$ and w is the vertical velocity at the interface. Following *Speer and McCartney* [1992], integrating equation (5) in x over the extent of the layer, assuming h is a constant on the eastern boundary, h_o, and choosing $f = \beta y$, then gives

$$h^2(x,y) = h_o^2 - \frac{2\beta w}{g'} x' y^2, \tag{6}$$

with transport solutions of

$$hv = wy \tag{7}$$

$$hu = 2wx', \tag{8}$$

where $x' = L - x$. Thus there is an explicit connection between the bottom layer transport and the diapycnic vertical velocity, w, which is defined by the reference thickness of the bottom layer h_o and source strength of the bottom water, S_o:

$$w = \frac{\gamma S_o}{4L^2} \left(\frac{1}{\gamma} + 1 \right)^2, \tag{9}$$

where $\gamma = g' h_o^2/(\beta S_o L)$, which is modified from *Speer and McCartney* [1992] to take into account parameters for the Pacific; $g' = 6 \times 10^{-4}$ m s^{-2}, $\beta = 2 \times 10^{-11}$ m^{-1}s^{-1} and L = 5500 km.

[19] The model is forced by different strengths of bottom water source, S_o, from 13 Sv to 6 Sv for different choices of layer thickness, h_o, from 500 m to 1000 m with h constant along the equator; these different choices are broadly taken from the observed height of the σ_4 interfaces of 45.90 and 45.87 respectively (Figure 1a). The diapycnic vertical velocity out of the layer is assumed to be constant in space and is diagnosed from equation (9).

[20] The idealized model suggests that the thickness of the bottom layer decreases westward and northward over the interior of the northern basin (Figure 3a). If the diapycnic volume flux is increased, then the layer thins and grounds more rapidly westward and northward due to the transfer of mass into the overlying layer (Figure 3b). Thus reducing the diapycnic volume flux leads to a greater northward penetration of the bottom water over basin. Whether the layer actually grounds depends on the initial layer thickness h_o on the equator and eastern boundary, the strength of the diapycnic volume flux, and size of the basin (Figures 3a and 3b).

[21] While this solution for the layer thickness and accompanying flow field is overidealized through the lack of topographic variations and more moving layers, we expect that the sense of the relationship between layer thickness, grounding and diapycnic volume flux will still carry over for a more complex model (as investigated in section 4).

3.2. Radiocarbon Distribution

[22] We now explore the implications of the variation in the bottom water transport for a tracer, c, which is assumed broadly analogous to $^{14}C/^{12}C$. Here, we assume that there are two regimes. Firstly, in the bottom layer, the tracer is assumed to be controlled by the horizontal transport and the lateral boundary conditions, rather than by the decay. Hence the tracer concentration in the modeled bottom layer can be solved from the tracer equation at a steady state:

$$\frac{\partial}{\partial x}(huc) + \frac{\partial}{\partial y}(hvc) = -wc, \tag{10}$$

where in this highly idealized representation of the bottom waters the radio decay is assumed negligible. Combining with equations (7) and (8), equation (10) reduces to

$$2x' \frac{\partial c}{\partial x} + y \frac{\partial c}{\partial y} = 0, \tag{11}$$

which has a particular solution for the tracer concentration in the bottom layer of

$$c(x,y) = c_a + c_b x' y^2, \tag{12}$$

while the general solution for $c(x, y)$ is an arbitrary function of $x'y^2$. Additional boundary conditions are needed to determine the coefficients c_a, c_b. Here, we solve for c within the bottom layer with northern and southern boundary conditions taken from the observations: $c_a = 0.782$ at $y = 0$ and $c_b = 0.765$ at $x = L/2$ and $y = L$, which corresponds respectively to $\Delta^{14}C = -218$ at the equator and $\Delta^{14}C = -235$ at 170°W, 50°N (Key et al., submitted manuscript, 2004).

[23] Secondly, in the overlying deep waters, the tracer is assumed to be controlled by an advective-diffusive and

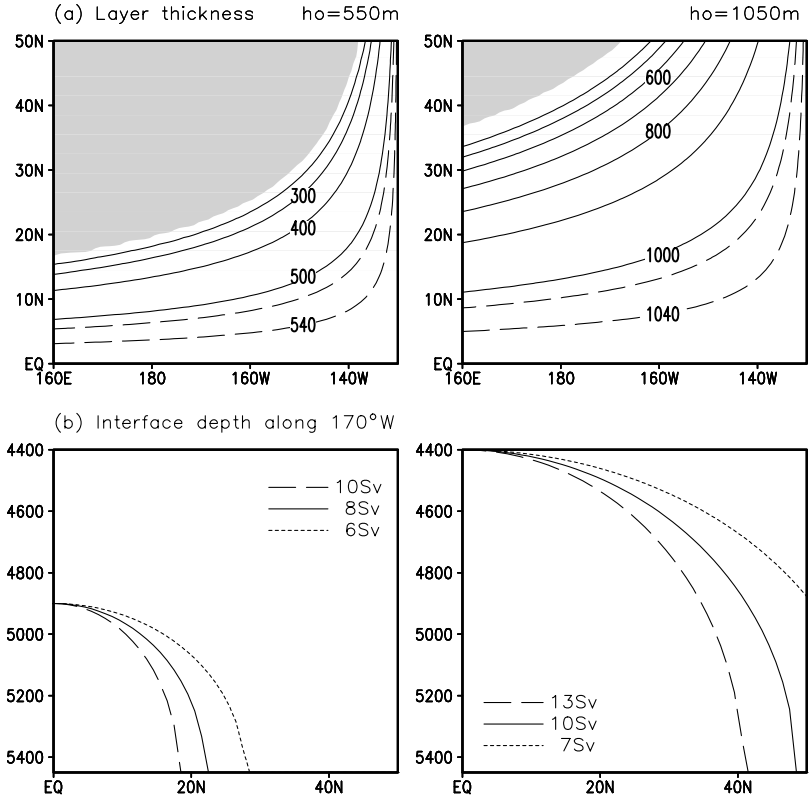

Figure 3. Idealized spreading of bottom water into a northern basin using a one-and-a-half-layer model: (a) a plan view of the bottom layer thickness for the model and (b) the interface height along 170°W for two different choices of layer thickness on the eastern boundary, h_o = 500 m and 1000 m in the left and right panels, respectively. In Figure 3b, the diapycnic volume flux for h_o = 500 m (left) decreases from 10 Sv, 8 Sv to 6 Sv for the overmixed (dashed line), optimal (solid line) and undermixed (dotted line) cases, respectively, and likewise for h_o = 1000 m (right) from 13 Sv, 10 Sv to 7 Sv. These two different choices in h_o are chosen to be comparable to the σ_4 = 45.90 and 45.87 surfaces in Figure 1a.

decay balance in the vertical, but with horizontal transport now ignored. Thus the vertical balance is given by

$$-w\frac{dc}{dz}+\kappa\frac{d^2c}{dz^2}+\lambda c=0, \tag{13}$$

where horizontal transport is only important indirectly through the bottom tracer boundary condition. The analytical solution for the tracer profile c is given by

$$c(z)=c_1\exp\Big(\Big(1+(1+\alpha)^{1/2}\Big)z/z^*\Big) + c_2\exp\Big(\Big(1-(1+\alpha)^{1/2}\Big)z/z^*\Big)\Big), \tag{14}$$

where $z^* = 2\kappa/w$ and $\alpha = 4\lambda\kappa/w^2$. In case of nondecaying tracer (λ = 0), the solution reduces to the classical advective-diffusion balance: $c(z) = c_1 \exp(\frac{w}{\kappa}z) + c_2$. For radiocarbon, $\lambda = \ln(2)/\tau$ and τ is the Δ^{14}C half-life of 5730 years. Solutions to equation (14) in the vertical are obtained using a constant value of $c = {}^{14}C/{}^{12}C = 0.802$ at 1000 m (corresponding to $\Delta^{14}C = -198$) and the c for the bottom layer from equation (12) at a height given by equation (6) and w diagnosed from equation (9). In the vertical balance, the timescales are slower and the radio decay makes a first-order contribution. Thus the one-dimensional solutions combined with the horizontal variations in the bottom layer leads to a plausible modeled meridional section with a middepth minimum at around 2 km (Figures 4a and 4b).

[24] Altering the mixing in both the bottom layer transport model and the vertical advective-diffusive model in a consistent manner leads to opposing changes in the vertical profile of radiocarbon (Figure 4c). An increase in the mixing leads to a reduction in c in the bottom waters due the reduction in thickness of the bottom layer, but an increase in C above 3 km due to the enhanced vertical diffusion (Figure 4c, dashed line). Conversely, a decrease in the mixing leads to an increase in c in the bottom waters due its enhanced layer thickness, but a decrease in c above 3 km due to the weaker diffusion (Figure 4c, dotted line).

[25] The modeled radiocarbon distribution is subsequently examined in a more realistic setting after applying an isopycnic model to the Pacific, combined with an off-line radiocarbon model and examining its dependence on bottom mixing.

4. Physical Model and the Circulation

4.1. Formulation of Model

[26] The model experiments focus on the influx of dense fluid into a basin using an isopycnic model (MICOM 2.7

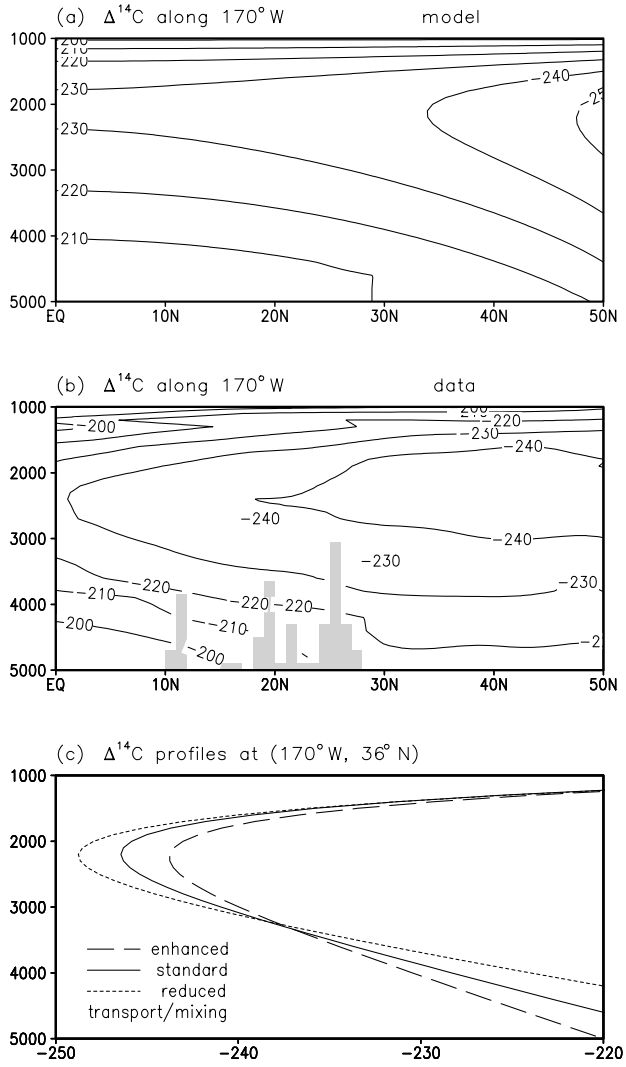

Figure 4. Vertical sections of $\Delta^{14}C$ along 170°W in the North Pacific for (a) an idealized model and (b) the data together with (c) a modeled vertical profile of $\Delta^{14}C$ at 170°W, 36°N. The idealized model solves firstly for the bottom layer transport of radiocarbon and secondly for the one-dimensional vertical advective, diffusive, and decay balance. In the one-dimensional vertical model the upper tracer boundary condition is taken from the observations at 1000 m, and the lower boundary condition is provided by the bottom layer transport model; the model solutions are shown for bottom layer thickness of h_o = 1000 m (Figure 3 (right)). In Figure 4c, different model solutions are shown for diapycnic volume fluxes of 13 Sv (dashed line), 10 Sv (solid line), and 7 Sv (dotted line). Note how a decrease in the diapycnic volume flux leads to a higher concentration of the tracer below 3 km.

[*Bleck and Smith*, 1990]). The model formulation is similar to that employed by *Roussenov et al.* [2002], except with increased vertical resolution and layer interfaces relaxed in the Southern Ocean to a realistic profile. The model resolution includes 7 layers in the vertical of σ_4 = 43.5, 45.0, 45.64, 45.76, 45.84, 45.90 and 45.94 (Figure 5a), and 1.4° Mercator grid in the horizontal. The model topography is based on ETOP05 data averaged within the model grid. Additional corrections are made using the 5 minute topography to ensure that model topography includes deep channels and trenches, such as the Izu-Ogasawara and Japan trenches between 29°N and 42°N. The model is forced with a monthly mean, wind stress from the COADS climatology. In the southern part of the domain, cyclic boundary conditions on the western and eastern sidewalls are included in order to simulate the Antarctic Circumpolar Current over the upper water column. Since the experiments are focussing on the influx and modification of dense water, the buoyancy forcing is confined to a southern relaxation zone, where model interfaces are relaxed to depths taken from an observed density profile.

[27] Diapycnic transfer occurs throughout the domain and is necessary to provide a conversion of dense bottom water into lighter deep and intermediate water. Diapycnic fluxes are applied over the interior to compensate for the input of dense water from the southern relaxation zone. Additional diapycnic mixing is introduced between the deepest two interfaces in order to mimic enhanced bottom mixing and which eventually leads to a grounding of the bottom layer at about 20°N. The additional bottom mixing can either be viewed as a crude parameterization of enhanced mixing over rough topography [*Polzin et al.*, 1997] or mimicking the diapycnic transfer implied from geothermal heating which might be important in the North Pacific [*Joyce et al.*, 1986].

[28] The overall effect of the diapycnic transfer can be considered in terms of an effective diapycnic diffusivity, κ, consisting of two parts: (i) a background value, κ_s, and (ii) an additional mixing along the bottom interface, κ_{bot}, varying inversely with buoyancy frequency N. In the bottom waters, each contribution is comparable with $\kappa_{bot} \sim 0.7 \times 10^{-4}$ m^2 s^{-1}. Since there are still few direct measurements of the diapycnic mixing rates in the ocean, we include sensitivity studies on how the radiocarbon distribution is controlled by the bottom mixing. In addition, the isopycnic model employs isopycnic mixing and thickness diffusion (using a diffusive velocity of 0.5 cm s^{-1} with Laplacian and biharmonic forms respectively), and deformation-dependent momentum mixing (using a mixing velocity of 1 cm s^{-1} with a background Laplacian dependence). The model is initialized with flat isopycnals (Figure 5a, dashed lines) except within the southern relaxation zone. The model reaches a dynamical steady state after 500 years integration.

4.2. Model Circulation and Assessment

4.2.1. Overturning Circulation

[29] At a steady state, there is a northward transport of dense bottom waters, spreading over the bottom two model layers, reaching 22 Sv at 50°S (20 Sv in the bottom layer). The transport of bottom water is progressively transformed to lighter fluid by the diapycnic mixing leading to dense interfaces deepening and eventually grounding over the northern basin (Figure 5a, solid lines). This conversion involves a combination of the background mixing (11 Sv) and the enhanced bottom mixing (9 Sv) at the bottom two interfaces (Figure 5a, arrows). The lighter fluid eventually is returned to the southern relaxation zone over the overlying water column with 5 Sv in each of the deep layers, σ_4 = 45.84 and 45.76, and 8 Sv in each of the intermediate

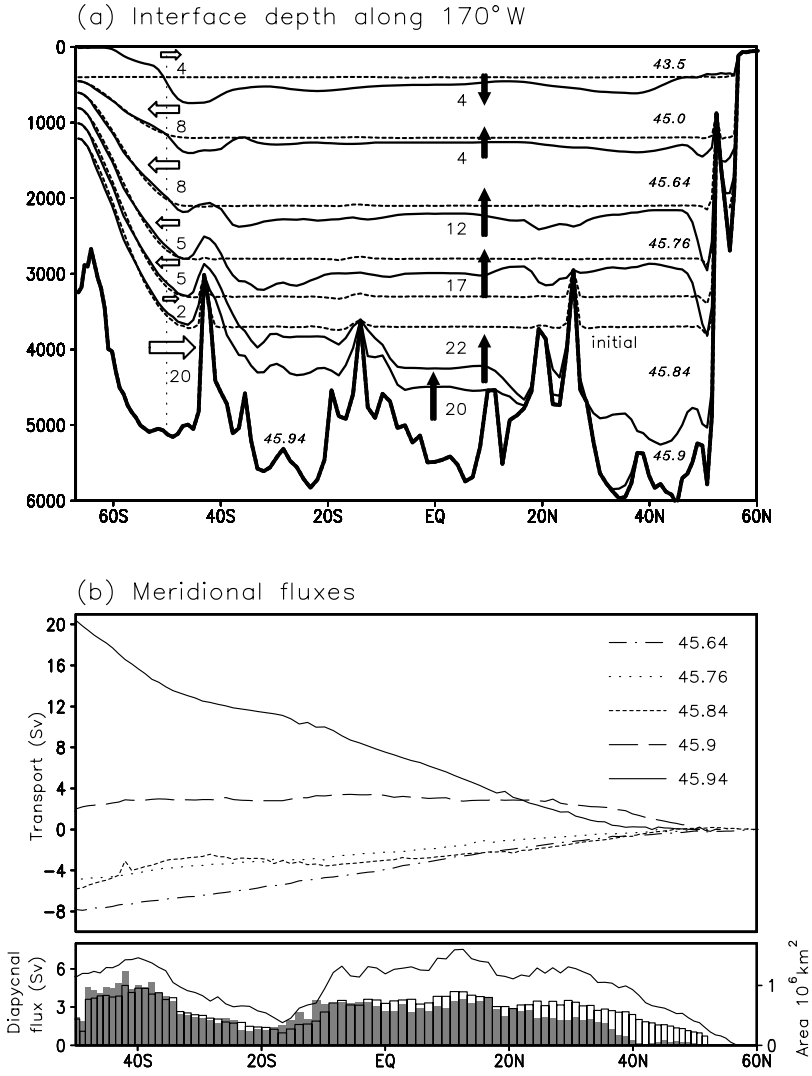

Figure 5. (a) Modeled meridional section for σ_4 along 170°W through the Pacific. The model is integrated for 500 years with realistic topography at 1.4° resolution and enhanced bottom mixing. The initial and final states are marked by the dashed and solid lines, respectively. There is a northward deepening of the denser interface. Arrows denoted the integrated meridional transport and diapycnic fluxes in Sv (1 Sv $\equiv 10^6$ m^3 s^{-1}). (b) The zonally integrated meridional fluxes for each of the denser layers north of 50°S at the final state. There is a northward influx of 22 Sv at 50°S carried over the bottom two layers, which is progressively transformed northward into the lighter layers and returned southward. In the bottom panel the area-integrated diapycnic flux (Sv) is included for each of the bottom two layers as bar charts (bottom layer is shaded) together with the surface area of the overlying model interface (solid line); the diapycnic flux is scaled to give the area-integrated mean flux in Sv for every 10° in latitude.

layers, σ_4 = 45.64 and 45.02. In addition, there is a northward flux of 4 Sv in the surface layer, which is balanced by a diapycnic transfer and return flow in the denser underlying layer.

[30] This transformation of dense fluid to light fluid occurs throughout the basin. The northward flux in the bottom layer (σ_4 = 45.94) progressively decreases from 20 Sv at 50°S to 0 at 35°N (Figure 5b, solid line), then the flux in the overlying layer (σ_4 = 45.9) decreases from 3 Sv at 35°N to 0 at the northern boundary (Figure 5b, long dashed line). The zonally integrated diapycnic flux (evaluated at the interface above the two bottom layers) varies according to the surface area of the interface (Figure 5b, bottom panel) with a minimum transfer at 20°S. Above the bottom interface, there is a weaker diapycnic transfer controlled by the background mixing.

4.2.2. Horizontal Circulation

[31] The wind forcing drives the expected upper layer, gyre-scale circulation with a western boundary current transport of 54 Sv in the Kuroshio for the northward flow across 24°N between the western boundary and 130°E. The Circumpolar Current transport through Drake Passage reaches 130 Sv. In comparison, *Ganachaud* [2003] using a global inverse model estimates 68 ± 7 Sv for the

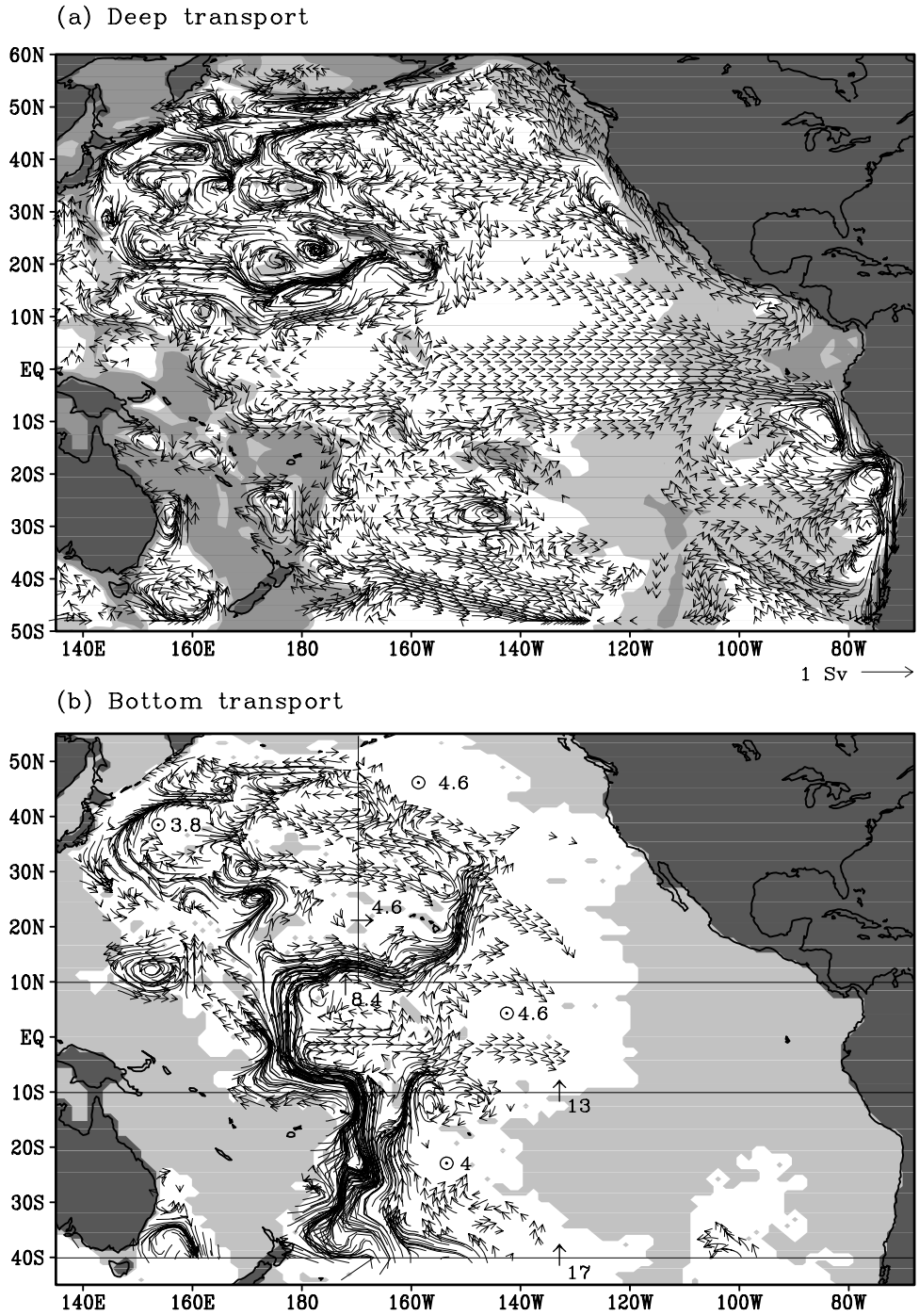

Figure 6. Modeled volume transports for (a) deep waters (σ_4 = 45.84 layer) and (b) bottom water (combined σ_4 = 45.90 and 45.94 layers) after 500 years integration. The vectors representing transport in the layer are scaled to 1 Sv (10^6 m^3 s^{-1}). In Figure 6a, dark and light shading represents depths less than 3 km and 4 km, respectively, while in Figure 6b, shading represents where the bottom two layers ground. In Figure 6b, values of the transport (Sv) are included within subregions of the domain together with the diapycnic flux into the lighter overlying layers.

Kuroshio transport and 140 ± 6 Sv through the Drakes Passage.

[32] The deep circulation (for the σ_4 = 45.84 layer) reveals a broadly zonal interior flow, directed eastward in the tropics, and an interior southward currents and recirculations at 50°N (Figure 6a). Over the western and eastern boundaries, there are northward transports over part of the northern basin, but change direction to southward transports over the southern basin. In the mid and deep waters, *Johnson and Toole* [1993] diagnose a southward transport of NPDW, −2.6 Sv, across 10°N, while the corresponding model transport, −3 Sv, is only slightly larger in magnitude.

In the deep waters, *Wijffels et al.* [2001] diagnose a southward deep water transport, −10 to −20 Sv at 32°S, while the model transport is southward, −6.4 Sv below 2200 m (for model layers σ_4 = 45.84 and 45.76) and −12.9 Sv below 1200 m (for model layers σ_4 = 45.84, 45.76 and 45.64).

4.2.3. Bottom Water Circulation

[33] Incorporating realistic topography leads to a complex bottom circulation including the formation of topographic jets and flow bifurcations (Figure 6b). The modeled northward transport of bottom water is carried principally by a deep western boundary current over the South Pacific, which reaches a maximum speed of 5–6 cm s^{-1}.

[34] Observations suggest that the northward transport for the bottom waters in the Pacific decreases northward from 16 to 20 Sv at 32°S from hydrographic data combined with an inverse model [*Wijffels et al.*, 2001] and 16 ± 12 Sv from current moorings (from 2 km to the bottom) at 32°S [*Whitworth et al.*, 1999], 12 Sv at 12°S [*Taft et al.*, 1991], 11.7 Sv from 11°S to 17°S [*Roemmich et al.*, 1996], 8.4 to 9.6 Sv at 10°N [*Johnson and Toole*, 1993] and 4.9 Sv at 24°N [*Bryden et al.*, 1991]. The model diagnostics show a very similar behavior with the bottom water transport, calculated as a zonal integral of the meridional fluxes in the deepest two model layers, σ_4 = 45.90 and 45.94, decreasing from 15.8 Sv at 32°S, 13 Sv at 12°S, 10.8 Sv at the equator, 8.4 Sv at 10°N to 5 Sv at 24°N.

[35] In more detail, the modeled boundary current bifurcates at 18°S with a branch separating from the coast, propagating northeast and transporting 3 Sv around the Manihiki Plateau (160°W, 10°S) (Figure 6b). The main western branch transports 11 Sv in the Samoan and Tokelau Passages (west of 170°W, 10°S). There is a southward transport of about 1 Sv across 10°S in the easternmost part of the basin (east of 155°W). The model western boundary transport and the total northward transport of 13 Sv across 10°S are very close to the observed 12 Sv of bottom water at 12°S [*Taft et al.*, 1991; *Roemmich et al.*, 1996] and a maximum of 10.7 Sv in the Samoan passage [*Rudnick*, 1997]. A small branch of the western boundary current (1 Sv) turns eastward in the equatorial region and recombines with the bottom waters east of Manihiki Plateau. However, most of the bottom waters transported across the equator (10.8 Sv) are carried by the western boundary current (9.8 Sv). The western boundary current bifurcates again north of the equator with one branch directed eastward, transporting 4.2 Sv through the Clarion passage (15°N, 170°W). This bifurcation is consistent with observations along 10°N by *Johnson and Toole* [1993].

[36] Further north, there is a complex circulation with the transport carried by interior jets following deep channels. North of 10°N, the total transport of bottom water eastward across 170°W is 4.6 Sv with 2.5 Sv carried along the deep channels between 25°N and 45°N. The model does simulate the northward current over the Izu-Ogasawara and Japan trenches (29°–40°N, 140°–160°E) as well as the southward countercurrent on the western side, which is diagnosed in the observations by *Owens and Warren* [2001]. Bottom currents eventually reaching the northern rim of the North Pacific are returned westward toward the western boundary.

[37] Over the large scale, the modeled circulation does not appear to be either consistently cyclonic, as expected from *Stommel and Arons* [1960] for a flat-bottom ocean, or anticyclonic as expected from the "hypsometric effect" suggested by *Rhines and MacCready* [1989]. Thus local changes in topography mask and obscure signatures of large-scale control of the horizontal circulation. The influence of the circulation patterns on the radiocarbon distribution is discussed next.

5. Radiocarbon Model and Tracer Distributions

5.1. Formulation of Model

[38] The dynamical model reaches a steady state after about 500 years, where there is a balance between the dense water inflow and the diapycnic transformation to lighter waters. The radiocarbon evolution takes much longer to reach a steady state due to the long half-life of radiocarbon requiring a model integration of several thousand years. Consequently, for computational efficiency, the radiocarbon distributions are modeled in an off-line mode. The off-line model has the same resolution and topography as the on-line model, and is driven using the transports and model fluxes taken from the dynamical model for a 5 year time average after 500 years integration. A general tracer, c, in the off-line model is governed by the prognostic equation

$$\frac{\partial c}{\partial t} + \mathbf{u}.\nabla c = \frac{1}{h}\nabla \cdot (\kappa h \nabla c), + S_c, \qquad (15)$$

where S_c represents sources and sinks including restoring boundary conditions in the surface layer and southern boundary regions, $\mathbf{u}$ is the three-dimensional velocity, h is the layer thickness and κ is the diffusivity providing diapycnic and isopycnic fluxes. Diapycnic fluxes are calculated using mixing coefficients varying with buoyancy frequency, obtained from the vertical profiles of the steady dynamical model solution.

[39] Radiocarbon is generally reported in terms of $\Delta^{14}C$ [*Stuiver and Polach*, 1977]. Rather than explicitly incorporate the biological carbon and radiocarbon pumps, we formulate an abiotic approach following the approach taken in the OCMIP studies (J. Orr et al., unpublished manuscript, 2000) (http://www.ipsl.jussieu.fr/OCMIP/phase2/simulations/Abiotic/HOWTO-Abiotic.html). However, this assumption neglects the biological input associated with dissolution of surface derived carbonate particles (either in the water column or on the bottom); *Fiadeiro* [1982] estimated that this source accounted for a 5% contribution for $\Delta^{14}C$, which was incorporated in a box model by *Srinivasan et al.* [2000].

[40] Two prognostic tracers are carried in the model integrations, abiotic dissolved inorganic carbon-12 concentration, $^{12}C_{sol}$, and abiotic dissolved inorganic radiocarbon concentration, $^{14}C_r$, which is scaled by the reference ratio $\gamma_r = (^{14}C/^{12}C)_{ref}$. Tracer equations (15) are integrated for $^{12}C_{sol}$ with no interior sources or sinks, and for $^{14}C_r$ with an interior sink from the radiocarbon decay with a half-life of 5730 years. The surface and southern boundary tracer concentrations for abiotic $^{12}C_{sol}$ and $^{14}C_r$ are broadly in accord with the observed DIC, alkalinity (Key et al., submitted manuscript, 2004) and oxygen [*Conkright et*

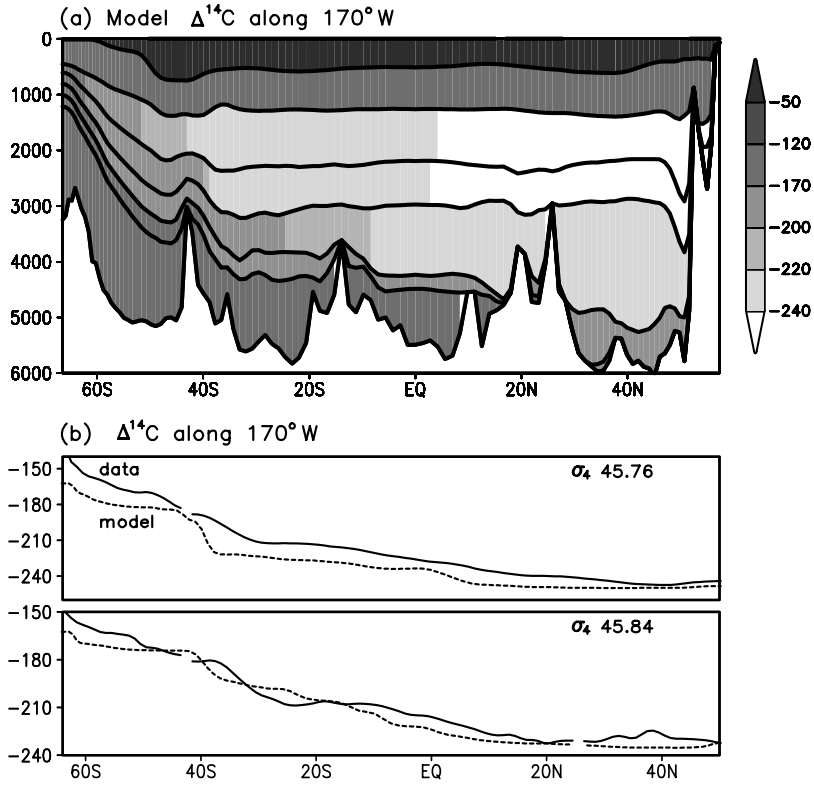

Figure 7. Modeled radiocarbon distribution for optimal mixing (equivalent to a bulk value for the diapycnic diffusivity $\kappa = 0.7$ cm^2 s^{-1}). (a) South-north section, Δ^{14}C (‰), along 170°W (compare with Figure 1b for the observations). There is an influx of radiocarbon into the domain from the surface and the transport of bottom waters from the southern boundary. (b) Meridional variation of Δ^{14}C along 170°W along $\sigma_4 = 45.76$ and 45.84 surfaces for both the observations (solid line) and model (dashed line).

al., 1998] climatologies (Appendix A). The boundary conditions are chosen as $^{12}C_{sol} = {}^{14}C_r = 2080$ in the mixed layer, $^{12}C_{sol} = 2125$ and $^{14}C_r = 1780$ in the relaxation zone in the southern boundary and $^{12}C_{sol} = 2110$ and $^{14}C_r = 1780$ initially in the interior. Finally, Δ^{14}C is diagnosed from these two tracers using the following relationship:

$$\Delta^{14}C_{model} = \left(\left(\frac{^{14}C_r}{^{12}C_{sol}} \right) - 1 \right) 1000. \qquad (16)$$

The boundary conditions imply $\Delta^{14}C = 0$ in the mixed layer, $\Delta^{14}C = -162$‰ in the southern boundary and initially $\Delta^{14}C = -156$‰ in the interior. This method of using two tracers explicitly accounts for nonlinear mixing effects which would otherwise be missed using a single tracer representing Δ^{14}C. The off-line tracer equations are integrated for 5000 years and there are only relatively minor changes between years 3000 and 5000.

5.2. Vertical Structure for Radiocarbon

[41] After 5000 years, the modeled radiocarbon distribution reproduces the general character of the observations: high surface values over the main thermocline, $\Delta^{14}C \sim -50$‰, an influx of lower values in the bottom waters from the southern boundary, $\Delta^{14}C \sim -170$‰, and a middepth minimum at 2 km in the North Pacific north of 40°N, $\Delta^{14}C \sim -240$‰ (Figure 7a). There is good agreement between the meridional variation in Δ^{14}C in the deep waters from the model and the observations (Figure 7b for $\sigma_4 = 45.76$ and 45.84).

[42] A separate ideal "age" calculation (not shown) reveals low ages in the thermocline and within the bottom waters spreading from the southern boundary, and a maximum age of 1400 years at middepths north of 10°N. There is a plume of relatively low ages reaching 600 years in the bottom waters extending into the North Pacific ($\sigma_4 = 45.94$) and increasing to 1000 years in the overlying layer ($\sigma_4 = 45.90$) with the greatest age along the eastern Pacific, while in the deep waters, the age reaches a maximum of 1400 years in the central part of the North Pacific ($\sigma_4 = 45.76$).

[43] An observed west-east section of Δ^{14}C reveals the northward flux of LCDW linked to the western boundary with young values (Figure 8a). The return flow of NPDW with old values appears to be concentrated into two cores at depths centered on 2500 m: one which is over the western Pacific and a second which abuts the western slope of South America. The eastern core is also seen in silicate [*Key*, 2001] and, perhaps, is also consistent with diagnostics of a southward transport of NPDW across 10°N east of 115°E [*Johnson and Toole*, 1993].

[44] In comparison, the model reveals the northward influx of young Δ^{14}C in the bottom waters along the western boundary (Figure 8b). There is reasonable agreement between the modeled and observed tracer values for

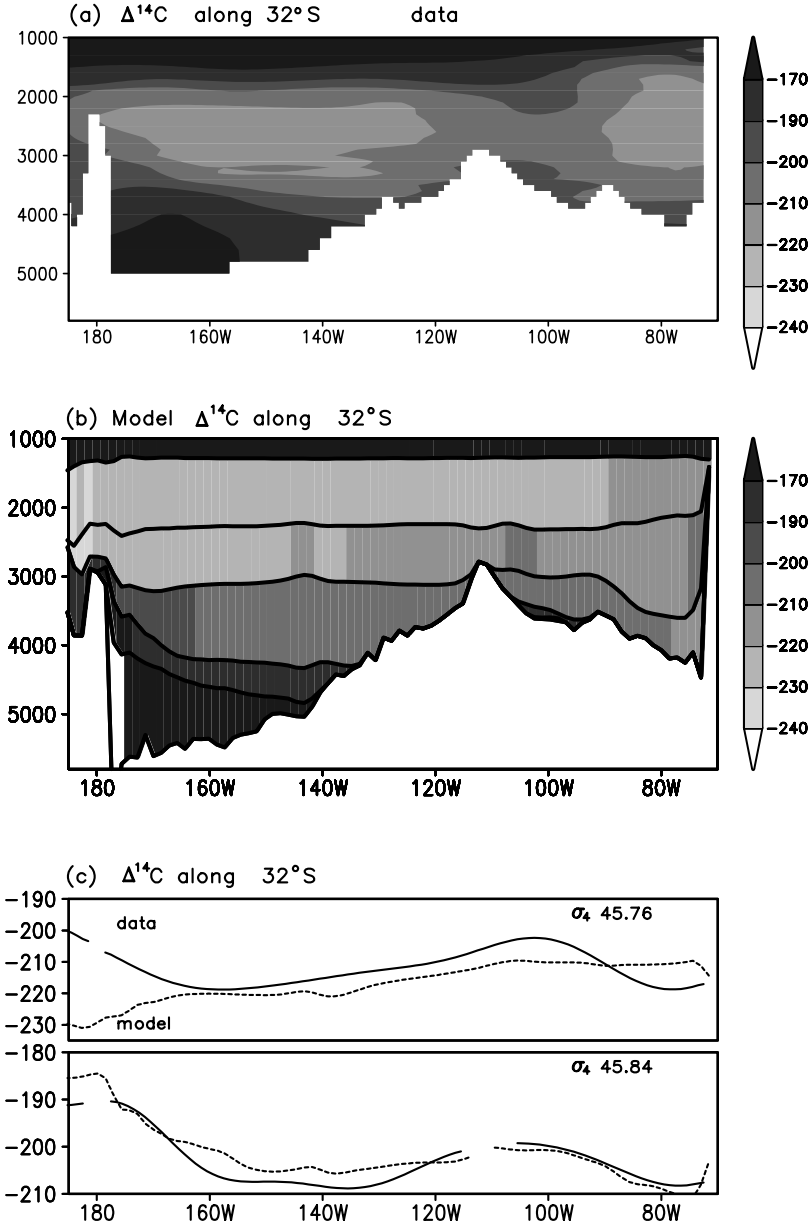

Figure 8. Radiocarbon west-east sections, $\Delta^{14}C$ (‰), along 32°S from (a) the observations and (b) the tracer model for optimal mixing. (c) Zonal variation of $\Delta^{14}C$ along 32°S for σ_4 = 45.76 and 45.84 surfaces from the observations (solid line) and model (dashed line).

the bottom waters, but disagreement for the lighter layers (along $\sigma_4 = 45.76$) along the western and eastern boundaries (Figure 8c). This disagreement is principally due to the modeled northward influx of young $\Delta^{14}C$ being too restricted to the bottom waters and the southward outflux of deep waters being concentrated in the western boundary, rather than within the central part of the basin or the eastern boundary as in the observations.

5.3. Horizontal Structure of Radiocarbon

[45] The $\Delta^{14}C$ pattern on the deep σ_4 surfaces reflects the pattern of the deep circulation and boundary flows, which in turn are partly controlled by the bottom topography (Figures 9a and 9b). The broad structure of the modeled $\Delta^{14}C$ is in general accord with the observations for the deep and bottom flows, but there are differences at middepths, perhaps reflecting the coarse model resolution in the vertical.

[46] For the deep waters along $\sigma_4 = 45.76$, $\Delta^{14}C$ is nearly uniform over the North Pacific with a minimum value of −250‰ reflecting a lack of ventilation (Figure 9a). Over the South Pacific, the $\Delta^{14}C$ contours extend from the southwest to northeast reflecting the southward transport of older waters from the North Pacific along the deep western boundary current, in accord with the transport pattern in Figure 6a for a similar σ_4 surface.

[47] As the density increases to 45.87, the pattern of the $\Delta^{14}C$ contours changes and acquires a northwest to southeast alignment over the entire basin (Figure 9b) (the $\Delta^{14}C$ along the model interface σ_4 = 45.87 is interpolated from

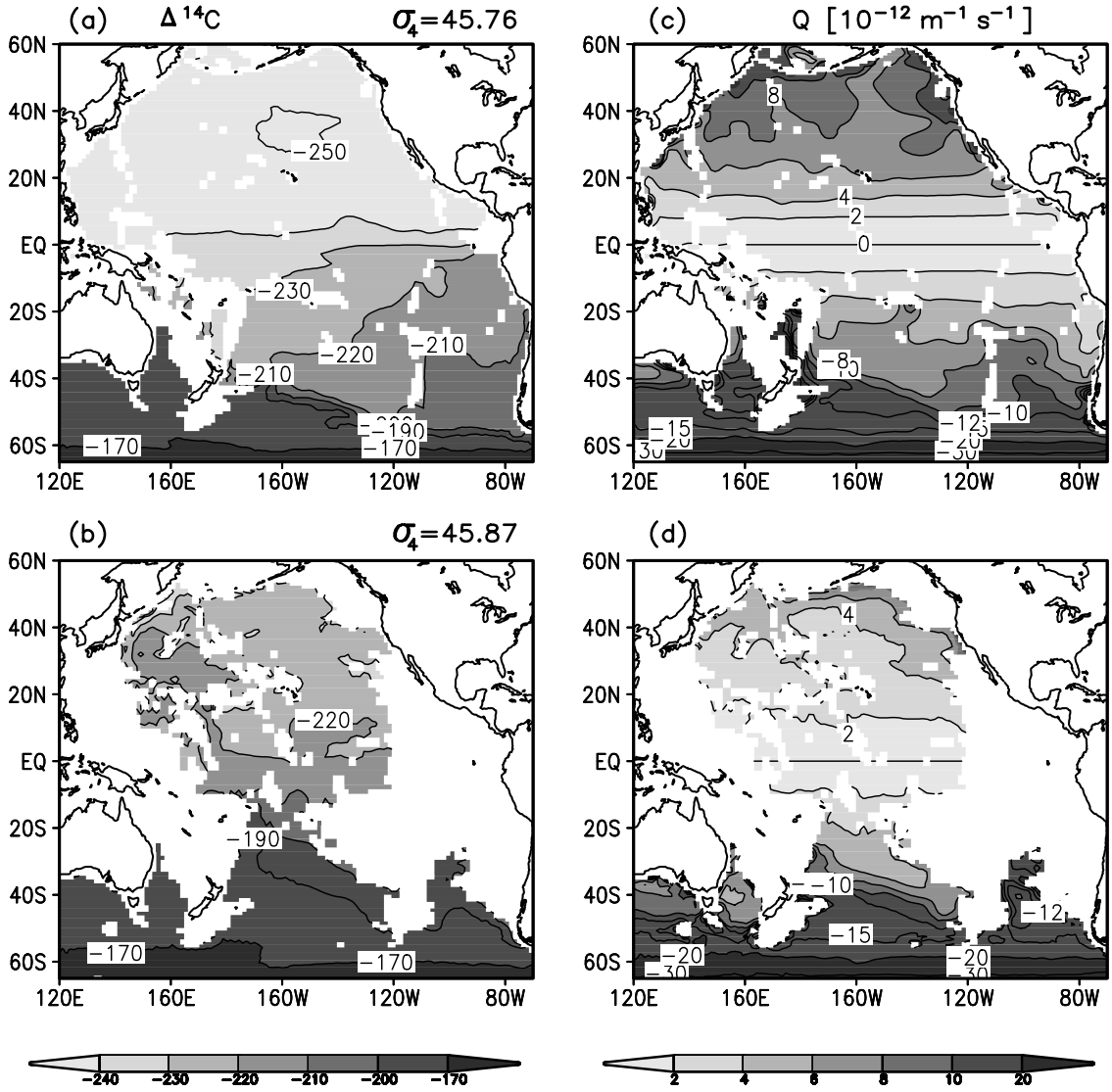

Figure 9. Modeled maps of $\Delta^{14}C$ (‰) for (a) σ_4 = 45.76 and (b) 45.87 surfaces, together with the potential vorticity (10^{-12} m^{-1} s^{-1}) for (c) σ_4 = 45.76 and (d) 45.87 surfaces. The $\Delta^{14}C$ distribution is after 5000 years of off-line integration, and the PV is after 500 years of on-line integration. The model solution reveals weaker meridional contrast in PV across the northern basin for the denser surface, which is broadly in accord with the diagnostics from the climatology (Figures 2c and 2d).

the concentrations in the neighboring layers). This change in orientation reflects the change in western boundary transport (Figure 6). The northward influx of dense bottom waters provides a corresponding influx of younger waters with higher $\Delta^{14}C$ from the Southern Ocean. For the bottom layers, σ_4 = 45.87 and 45.90 (not shown), there is a plume of high $\Delta^{14}C$ over the western side of the South Pacific, more uniform low values over the western side of the North Pacific, and the minimum values over the eastern side of the North Pacific (Figure 9b). This tracer pattern reflects the tight nature of the western boundary over the South Pacific, the more confused topographically controlled boundary flows in the North Pacific and, possibly, a weaker influx into the eastern North Pacific.

[48] In comparison, the observations reveal a similar northward plume of high radiocarbon along the western side of the Pacific for the deep and bottom waters (Figures 2a and 2b); σ_4 = 45.76 for the South Pacific and σ_4 = 45.87 for the whole Pacific. A difference between the modeled and observed radiocarbon distributions is the orientation of the tracer contours differs in the deep waters (σ_4 = 45.76), which is northwest to southeast in the observations, but more uniform or directed southwest to northeast in the model. However, it is unclear whether this model-data difference is significant, since there is little data there and comparable differences are formed using different mapping algorithms for the data.

5.4. Relationship Between Radiocarbon and PV Distributions

[49] In comparison, the model distributions of PV are evaluated, where the PV is based on a layer version of equation (1):

$$\mathrm{PV} = -\frac{(\zeta + f)}{h}\frac{\Delta\rho}{\overline{\rho}}. \qquad (17)$$

For completeness, the relative vorticity, ζ, is included, although this term is generally small; h is the thickness of an isopycnal layer, $\Delta\rho$ is the density difference between the interfaces bounding the isopycnal layer and $\overline{\rho}$ is a reference density.

[50] The modeled PV distribution shows predominately zonal contours along $\sigma_4 = 45.76$ (Figure 9c) with a generally symmetric pattern between the North and South Pacific. On the denser 45.87 surface, the most striking signal is the much weaker contrasts in PV over the North Pacific and the PV contours become more inclined away from latitude circles over the western side of the South Pacific (Figure 9d), which is also seen in the data (Figures 2c and 2d). The extensive region of low and nearly uniform PV over the North Pacific is explained in terms of an influx of fluid into the isolated northern basin from across the equator together with enhanced bottom mixing [*O'Dwyer and Williams*, 1997; *Roussenov et al.*, 2002]. Alternatively, this signal of low PV might result from geothermal heating leading to a weakening in stratification [*Joyce et al.*, 1986].

[51] The radiocarbon and PV distributions offer complementary views of the deep circulation. Their patterns do not directly reflect each other, so one tracer is not a redundant proxy for the other tracer, but there are some similarities in their patterns given the controlling influence of the background circulation.

[52] Over the South Pacific, the radiocarbon distribution reflects the influence of the western boundary current transport with the orientation of the tracer contours changing from being aligned southwest/northeast for the deep waters (Figure 9a) to northwest/southeast for the bottom waters (Figure 9b). The PV has a similar pattern in the bottom waters, but only a limited signal of the southward transport in the western boundary in the deep waters (Figure 9c). Since the North Pacific is a more isolated basin, there are generally weaker tracer contrasts, than in the South Pacific. $\Delta^{14}C$ is more uniform for intermediate and deep waters (Figure 9a), while PV is more uniform for the layer within which the bottom water spreads northward into the basin (Figure 9d).

[53] The different signals in the radiocarbon and PV distributions might partly reflect how the radiocarbon only depends on the circulation in a particular layer, whereas the PV depends on the separation of layer interfaces, which are directly connected to the flow in the neighboring layers.

6. Model Sensitivity to Bottom Mixing

[54] Recent observations indicate increased rates of diapycnic mixing toward the bottom of the ocean and over rough topography [*Polzin et al.*, 1997]. In addition, geothermal heating can weaken the stratification and alter the deep transports; *Adcroft et al.* [2001] find that including 50 mW m^{-2} of geothermal heating increases the deep Indian-Pacific circulation by 1.8 Sv. The inclusion of bottom intensified mixing improves the hydrographic structure in idealized models of the deep Pacific basin [*Roussenov et al.*, 2002], but is not usually applied in ocean tracer models.

[55] In the previous idealized model, we explored the sensitivity of the transport and radiocarbon distribution to mixing given several simplifying assumptions, such as a flat bottom, no tracer decay in the bottom water and no horizontal transport within the ocean interior. The role of mixing is now reexamined using the more realistic circulation model.

6.1. Dynamical Response of Hydrography

[56] Firstly, we consider how altering the diapycnic mixing changes the volume fluxes and hydrography within the dynamical model. Secondly, we consider how changes in diapycnic mixing alter the radiocarbon distribution, both passively from the diffusion of radiocarbon and dynamically from the tracer transport.

[57] In these sensitivity experiments, the bulk diapycnic diffusivity, κ is altered from the standard value of 0.7 cm^2s^{-1} to either 0.5 or 1.0 cm^2s^{-1}. We refer to these as the "undermixed" and "overmixed" cases respectively. In these dynamical integrations, increases in mixing rate alter the structure of the bottom waters (Figure 10a): there is a more rapid northward deepening of the dense σ_4 surfaces for stronger mixing and flatter surfaces for weaker mixing.

[58] The different choices in bottom mixing alters the strength of the bottom water source, as well as the detail of the meridional fluxes within the bottom two layers (Figure 10b). At 50°S, the meridional flux in the bottom layer increases from 20 Sv for the standard case to 22 Sv in the overmixed case and decreases to 18 Sv in the undermixed case. However, the greater diapycnic transfer causes the meridional flux to decrease northward more rapidly for the overmixed case, than for the undermixed case. Consequently, the bottom flux and supply of bottom waters reaching the North Pacific is greater in the undermixed case, than the overmixed case (despite the bottom water source at the southern boundary being larger for the overmixed case). These different volume fluxes alter the volume of the bottom layer, and hence alter the surface area of the overlying interface over the North Pacific (Figure 10c). In the undermixed case, the interfaces of the bottom waters are flatter, while in the overmixed case, the interfaces ground further south and there is less bottom water in the North Pacific (Figure 10a). Thus the area-averaged diapycnic flux is much greater for the undermixed case in the North Pacific and occurs higher up the water column, than for the overmixed case.

6.2. Sensitivity of Radiocarbon Distributions

[59] We now discuss sensitivity experiments with enhanced or weakened diapycnic mixing with imposed diapycnic diffusivities of κ = 1.0, 0.7 (corresponding to the control model integration) and 0.5 cm^2s^{-1}. The accompanying bottom transport is either chosen to remain unchanged (in an off-line manner with the same model circulation) or altered in accord with the mixing (with the source of bottom water at the southern boundary greater with stronger mixing).

[60] For a strengthening in the diapycnic mixing, there is an overall increase in the $\Delta^{14}C$ over the northern basin (Figures 11a and 11b) due to the greater diffusive supply from the surface and bottom water. For a weakening in the diapycnic mixing, there are different results according to whether the accompanying bottom water transport is altered (Figures 11c and 11d). If the bottom water transport is unchanged, the middepth minimum in $\Delta^{14}C$

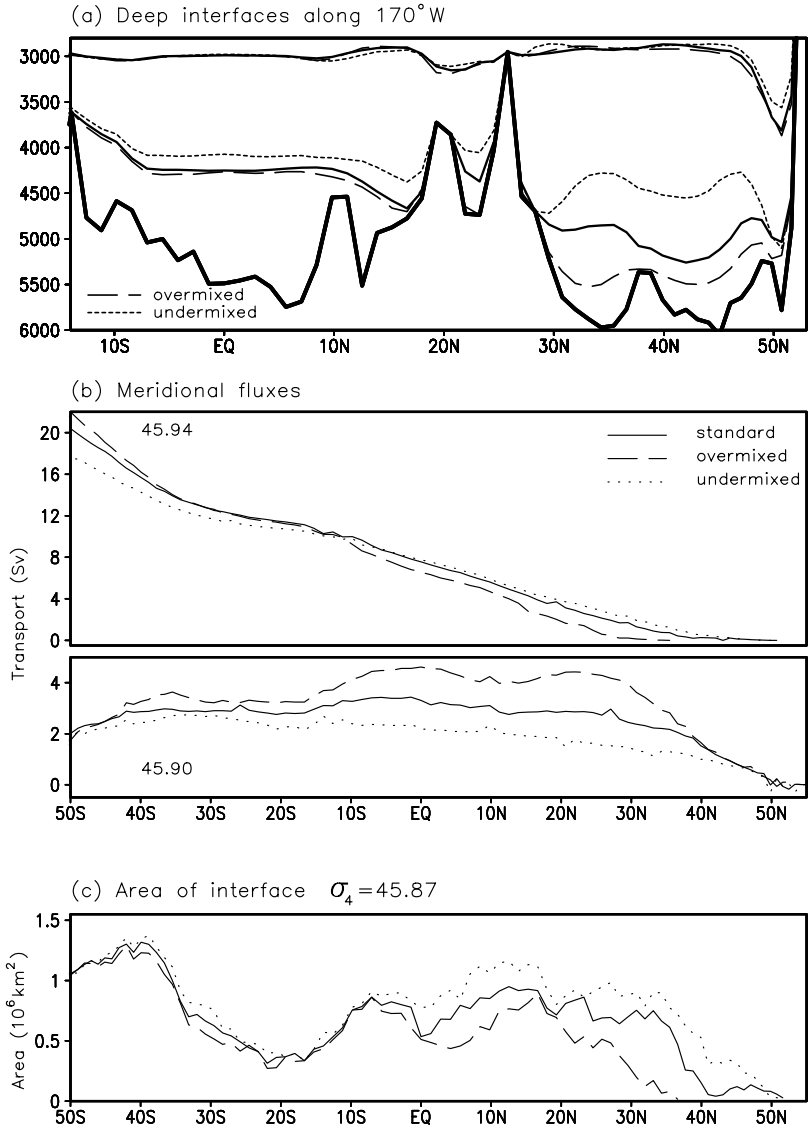

Figure 10. (a) Meridional section along 170°W showing the vertical positions of the σ_4 = 45.80 and 45.87 for different choices of bottom mixing and strength of the bottom water source: standard, optimal case, overmixed with stronger bottom water source, and undermixed with weaker bottom water source (solid, dashed, and dotted lines, respectively). (b) Zonally integrated meridional flux for each of the bottom two layers (σ_4 = 45.94 and 45.90, upper and lower panels, respectively) for the different mixing/transport cases. (c) Surface area of the interface σ_4 = 45.87. Note that to emphasize the different heights of σ_4 surfaces, Figure 10a is only shown from 14°S to 53°N, while Figures 10b and 10c are from 50°S to 55°N.

progressively decreases as the supply of tracer is reduced (Figures 11c and 11e). However, if the bottom water transport is allowed to alter with a weakening in diapycnic mixing, then there is younger (less negative Δ^{14}C waters in the northern basin (Figures 11d and 11f). This surprising signal is due to there being a greater northward extent of the radiocarbon-rich, bottom waters for weak mixing (Figure 10a).

[61] In the bottom water, the modeled meridional distribution of Δ^{14}C is optimal for our default choice of mixing and the agreement with the observations is degraded by either decreasing or increasing the diapycnic mixing (Figure 12). In the overlying water, such as σ_4 = 45.76, the data is close to the model results for the default choice of mixing north of 30°N, but is closer to the overmixed model case for the South Pacific, possibly reflecting the existence of regionally varying mixing in reality.

[62] There is reasonable agreement between the model responses for changes in mixing from the idealized, one-and-a-half-layer model and the isopycnic circulation model. Both models reveal that weak mixing leads an increased northward penetration of bottom water and thus an enhanced bottom supply of Δ^{14}C (Figures 4c and 11f, dotted line). There is a strong vertical decrease in Δ^{14}C with height due to the weak diffusive supply. Conversely, with stronger mixing, both models show a weaker vertical contrast in Δ^{14}C due to the stronger diffusive supply (Figures 4c and 11f, dashed

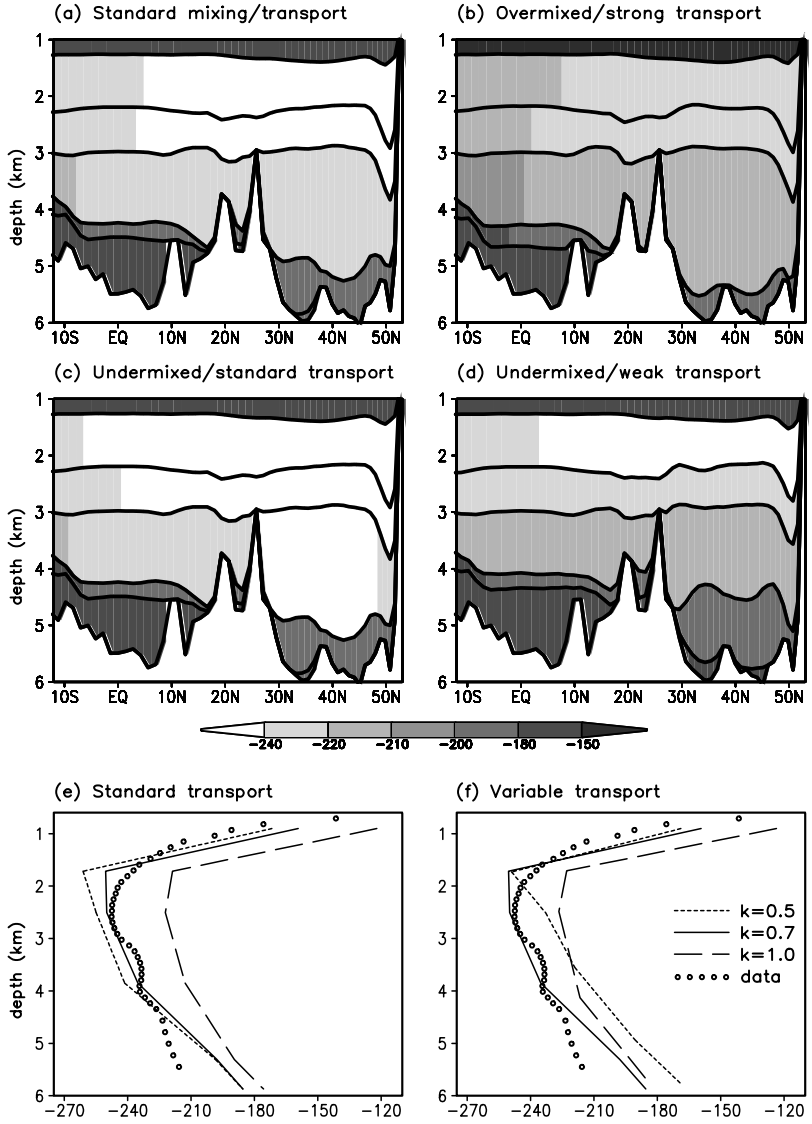

Figure 11. Modeled radiocarbon, $\Delta^{14}C$ (‰), sections along 170°W from 10°S to 50°N for different choices of bottom mixing and strength of the bottom water source: (a) standard, optimal case; (b) overmixed with stronger bottom water source; (c) undermixed with standard bottom water source (and artificially unchanged transport pattern); and (d) undermixed with weaker bottom water source. In addition, vertical profiles of $\Delta^{14}C$ are included at 36°N, 170°W for the observations (circles) and from the model for different choices in diapycnic diffusivity with (e) standard transport and (f) variable transport. The overmixing, standard mixing, and undermixing cases are equivalent to bulk values of diapycnic diffusivity of κ = 1.0, 0.7 and 0.5 $cm^2\ s^{-1}$ and are represented by dashed, solid, and dotted lines, respectively.

line). However, the models differ in the higher mixing case; the realistic model shows a supply of young $\Delta^{14}C$ in the bottom waters similar to the default case (Figure 11f), but otherwise differs due to the increased diffusive supply which dominates over the change in advection $\Delta^{14}C$ (Figures 11e and 11f, dashed line). This compensation is not captured in the idealized model.

7. Conclusions

[63] The radiocarbon distribution provides a useful tool to understand the deep ocean and the model representation of the transport and ventilation processes. In this study, the radiocarbon distribution in the deep Pacific is simulated, firstly, using a one-and-a-half-layer model for the bottom water in a northern basin with a vertical advective, diffusive and decay model, then secondly, in terms of a more realistic isopycnal circulation model coupled with radiocarbon sources and sinks. Two regimes control the radiocarbon distribution in the deep waters: a relatively fast horizontal transport of young $\Delta^{14}C$ in the bottom waters, and a much slower vertical balance between advection-diffusion and radioactive decay.

[64] The idealized model broadly captures the large-scale radiocarbon distribution, but its background circulation is too simple. Applying the more realistic isopynic model

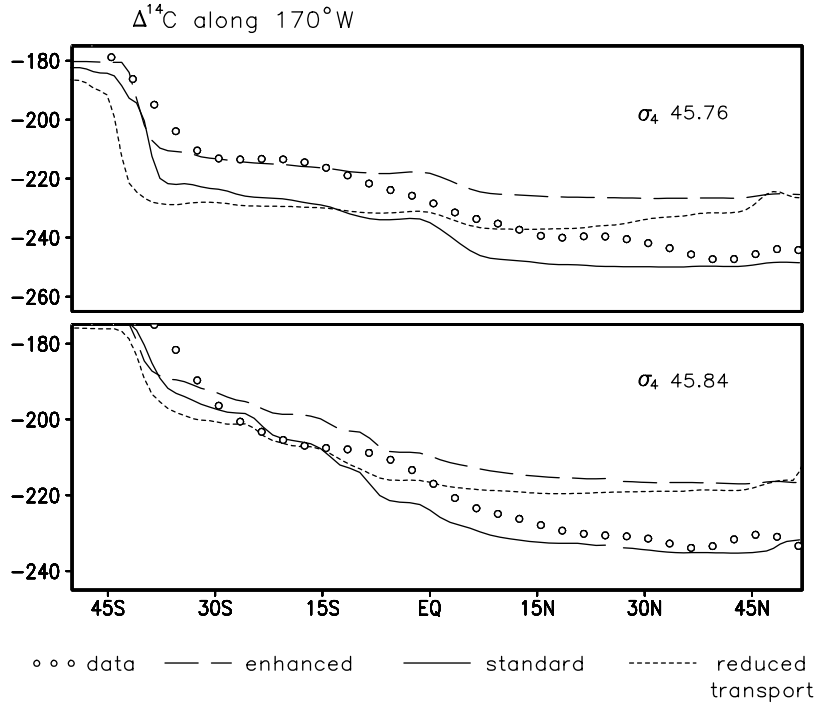

Figure 12. Meridional variation of observed (circles) and modeled $\Delta^{14}C$ along 170°W along 45.76 and 45.84 surfaces for different choices of bottom mixing and strength of the bottom water source. The standard, optimal, overmixed with stronger bottom water source, and undermixed with weaker bottom water source cases are represented by dashed, solid, and dotted lines, respectively.

reveals the strong topographic control of the deep circulation. The orientation of the $\Delta^{14}C$ contours along an isopycnic layer reflects the direction of the western boundary current and the transport of tracer into the basin. The modeled radiocarbon distribution shows good agreement with the observed distribution in the deep and bottom waters, but the model fails to simulate the southward spreading of older $\Delta^{14}C$ at middepths along the eastern boundary of the southern basin.

[65] Altering the imposed levels of bottom mixing changes both the local diffusive supply and the large-scale bottom transport of $\Delta^{14}C$. The idealized model illustrates how decreasing the mixing leads to a greater northward penetration of bottom water and young $\Delta^{14}C$ over the basin, while increasing the mixing reduces the northward extent of the bottom water. In the realistic model study, there is an optimal level of mixing where both increasing or decreasing the diapycnic mixing can degrade the agreement between the model results and observations for the bottom waters: increasing the diapycnic mixing leads to an increase in the diffusive supply of $\Delta^{14}C$, while decreasing the diapycnic mixing leads to a greater northward penetration of bottom water and injection of younger $\Delta^{14}C$ into the North Pacific.

Appendix A

[66] The surface and southern boundary tracer concentrations are restored toward abiotic ^{12}C and ^{14}C fields determined from observed DIC, alkalinity (Key et al., submitted manuscript, 2004) and oxygen [*Conkright et al.*, 1998] climatologies. "Abiotic" carbon in the boundary regions is estimated using the relationship of *Brewer* [1978], as applied by *Follows et al.* [1996]:

$$^{12}C_{sol} = {}^{12}C_{obs} - \frac{1}{2}\left(TA_{obs} - TA^{surf}\right) - \frac{115}{106}\left(O_{2(obs)} - O_2^{surf}\right),$$

where *TA* is alkalinity. The second term on the right adjusts for the remineralization of $CaCO_3$ in the water column and the third term on the right accounts for the remineralization of organic soft tissue. Fixed Redfieldian stoichiometry is assumed during biological transformations. Terms in brackets on the right represent differences between observed interior values and the values on those isopycnals at the point of ventilation of the water parcel into the thermocline. Oxygen is assumed to be close to saturation at the ocean surface and hence may be estimated from temperature and salinity, and TA^{surf} to be 2300 μmol kg^{-1}, a plausible choice for waters from a Southern Ocean surface source.

[67] The distribution of ^{14}C in the boundary regions is determined from the objectively mapped $\Delta^{14}C$ distribution (Key et al., submitted manuscript, 2004) assuming that

$$\gamma_{sol} = \gamma_r\left(\frac{\Delta^{14}C}{1000} + 1\right)$$

and

$$^{14}C_{sol} = {}^{12}C_{sol}\gamma_r\left(\frac{\Delta^{14}C}{1000} + 1\right),$$

where, following the usual definitions, $\gamma = {}^{14}C/{}^{12}C$, $\gamma_r = ({}^{14}C/{}^{12}C)_{reference}$ and $\delta^{14}C = (\gamma/\gamma_r - 1)1000$. It is convenient

to carry $^{14}C_r = {}^{14}C/\gamma_r$ in the model, following the OCMIP protocols (J. Orr et al., unpublished manuscript, 2000). Hence the target value derived from observations, and which the model restores toward in the surface and southern boundary waters, is scaled by γ_r. Over the interior, $^{14}C_r$ decays with a half-life of 5730 years.

[68] $^{12}C_{sol}$ has a general increase with depth as the solubility increases with reduced temperature, while $^{14}C_r$ is enhanced in the surface and bottom waters through the surface injection and bottom transport of radiocarbon. The $\Delta^{14}C$ distribution broadly follows that of $^{14}C_r$, but with a deeper middepth minimum due to $^{12}C_{sol}$ increasing with depth.

[69] **Acknowledgments.** The work was supported by a NERC RAPID research grant NER/T/S/2002/439 and a HEFCE JREI award in 1999 for a supercomputing cluster (NESSC) (R.G.W.), NSF grants OCE-0136609 (M.J.F.) and OCE-9986310, and NOAA grant NA96GP0200 (R.M.K.). The study benefited from the constructive comments of two anonymous referees.

References

Adcroft, A., J. R. Scott, and J. Marotzke (2001), Impact of geothermal heating on the global ocean circulation, *Geophys. Res. Lett.*, *28*, 1735–1738.

Bleck, R., and L. T. Smith (1990), A wind-driven isopycnic coordinate model of the north and equatorial Atlantic Ocean: 1. Model development and supporting experiments, *J. Geophys. Res.*, *95*, 3273–3285.

Brewer, P. G. (1978), Direct observation of the oceanic CO_2 increase, *Geophys. Res. Lett.*, *5*, 997–1000.

Broecker, W. S., T.-H. Peng, G. Ostlund, and M. Stuiver (1985), The distribution of bomb radiocarbon in the ocean, *J. Geophys. Res.*, *90*, 6953–6970.

Broecker, W. S., S. Sutherland, W. Smethie, T.-H. Peng, and G. Ostlund (1995), Oceanic radiocarbon: Separation of the natural and bomb components, *Global. Biogeochem. Cycles*, *9*, 263–288.

Bryden, H. L., D. H. Roemmich, and J. A. Church (1991), Ocean heat transport across 24°N in the Pacific, *Deep Sea Res.*, *38*, 297–324.

Conkright, M. E., S. Levitus, T. O'Brien, T. P. Boyer, J. I. Antonov, and C. Stephens (1998), *World Ocean Atlas 1998 CD-ROM Data Set Documentation*, *Tech. Rep. 15*, 16 pp., Nat. Oceanogr. Data Cent., Silver Spring, Md.

Fiadeiro, M. E. (1982), Three-dimensional modeling of tracers in the deep Pacific Ocean II. Radiocarbon and the circulation, *J. Mar. Res.*, *40*, 537–550.

Follows, M. J., R. G. Williams, and J. C. Marshall (1996), The solubility pump of carbon in the subtropical gyre of the North Atlantic, *J. Mar. Res.*, *54*, 605–630.

Ganachaud, A. (2003), Large-scale mass transports, water mass formation, and diffusivities estimated from World Ocean Circulation Experiment (WOCE) hydrographic data, *J. Geophys. Res.*, *108*(C7), 3213, doi:10.1029/2002JC001565.

Ishizaki, H. (1994), A simulation of the abyssal circulation in the North Pacific Ocean. Part II. Theoretical rationale, *J. Phys. Oceanogr.*, *24*, 1941–1954.

Johnson, G. C., and J. M. Toole (1993), Flow of deep and bottom waters in the Pacific at 10N, *Deep Sea Res.*, *40*, 371–394.

Joyce, T. M., B. A. Warren, and L. D. Talley (1986), The geothermal heating of the abyssal subarctic Pacific Ocean, *J. Phys. Oceanogr.*, *33*, 1003–1015.

Keffer, T. (1985), The ventilation of the world's oceans: Maps of the potential vorticity field, *J. Phys. Oceanogr.*, *15*, 509–523.

Key, R. M. (1996), WOCE Pacific Ocean radiocarbon program, *Radiocarbon*, *38*, 415–423.

Key, R. M. (2001), Ocean process tracers: Radiocarbon, in *Encyclopedia of Ocean Sciences*, edited by J. Steele, S. Thorpe, and K. Turekian, pp. 2338–2353, Academic, San Diego, Calif.

Key, R. M., P. D. Quay, G. A. Jones, A. P. McNichol, K. F. Von Reden, and R. J. Schneider (1996), WOCE AMS Radiocarbon I: Pacific Ocean results; P6, P16 & P17, *Radiocarbon*, *38*, 425–518.

Key, R. M., P. D. Quay, P. Schlosser, M. Stuiver, H. G. Ostlund, J. Hayes, A. P. McNichol, K. F. Von Reden, and R. J. Schneider (2002), WOCE Radiocarbon IV: Pacific Ocean results; P10, P13N, P14C, P18, P19 & S4P, *Radiocarbon*, *44*, 239–392.

McDowell, S., P. B. Rhines, and T. Keffer (1982), North Atlantic potential vorticity and its relation to the general circulation, *J. Phys. Oceanogr.*, *12*, 1417–1436.

O'Dwyer, J., and R. G. Williams (1997), The climatological distribution of potential vorticity over the abyssal ocean, *J. Phys. Oceanogr.*, *27*, 2488–2506.

Orr, J. (2002), Global storage of anthropogenic carbon (GOSAC), final report, EC Environ. and Clim. Prog., Paris.

Ostlund, H. G., and M. Stuiver (1980), GEOSECS Pacific radiocarbon, *Radiocarbon*, *22*, 25–53.

Owens, W. B., and B. A. Warren (2001), Deep circulation in the northwest corner of the Pacific Ocean, *Deep Sea Res., Part I*, *48*, 959–993.

Polzin, K. L., J. M. Toole, J. R. Ledwell, and R. W. Schmitt (1997), Spatial variability of turbulent mixing in the abyssal ocean, *Science*, *276*, 93–96.

Reid, J. L. (1997), On the total geostrophic circulation of the Pacific Ocean: Flow patterns, tracers and transports, *Prog. Oceanogr.*, *39*, 263–352.

Rhines, P. B., and P. M. MacCready (1989), Boundary control over the large-scale circulation, in *Parameterization of Small-Scale Processes*, edited by P. Mueller, pp. 75–99, Hawaii Inst. of Geophys. Spec. Publ., Univ. of Hawaii, Honolulu.

Roemmich, D., S. Hautala, and D. Rudnick (1996), Northward abyssal transport through the Samoan passage and adjacent regions, *J. Geophys. Res.*, *101*, 14,039–14,055.

Roussenov, V., R. G. Williams, and J. E. O'Dwyer (2002), Formation of low potential vorticity over the deep Pacific, *J. Phys. Oceanogr.*, *32*, 1811–1823.

Rudnick, R. L. (1997), Direct velocity measurements in the Samoan Passage, *J. Geophys. Res.*, *102*, 3293–3302.

Speer, K. G., and M. S. McCartney (1992), Bottom water circulation in the western North Atlantic, *J. Phys. Oceanogr.*, *22*, 83–92.

Srinivasan, A., C. G. H. Rooth, Z. Top, and D. B. Olson (2000), Abyssal upwelling in the Indian Ocean: Radiocarbon diagnostics, *J. Mar. Res.*, *58*, 755–778.

Stommel, H., and A. B. Arons (1960), On the abyssal circulation of the world ocean—II. An idealized model of the circulation pattern and amplitude in oceanic basins, *Deep Sea Res.*, *6*, 217–233.

Stuiver, M., and H. A. Polach (1977), Discussion: Reporting of 14C data, *Radiocarbon*, *19*, 355–363.

Stuiver, M., G. Ostlund, R. M. Key, and P. J. Reimer (1996), Large volume WOCE radiocarbon sampling in the Pacific Ocean, *Radiocarbon*, *38*, 519–561.

Taft, B. A., S. P. Hayes, G. E. Friederich, and L. A. Codispoti (1991), Flow of abyssal water into the Samoan Passage, *Deep Sea Res.*, *38*, suppl., 103–128.

Talley, L. D., and T. M. Joyce (1992), The double silica maximum in the North Pacific, *J. Geophys. Res.*, *97*, 5465–5480.

Thompson, L., and G. C. Johnson (1996), Abyssal currents generated by diffusion and geothermal heating over rises, *Deep Sea Res., Part I*, *43*, 193–211.

Toggweiler, J. R., K. Dixon, and K. Bryan (1989), Simulations of radiocarbon in a coarse-resolution world ocean model I: Steady-state, prebomb distributions, *J. Geophys. Res.*, *94*, 8217–8242.

Whitworth, T., III, B. A. Warren, W. D. Nowlin Jr., S. B. Rutz, R. D. Pillsbury, and M. I. Moore (1999), On the deep western-boundary current in the southwest Pacific Basin, *Prog. Oceanogr.*, *43*, 1–54.

Wijffels, S. E., J. M. Toole, and R. Davis (2001), Revisiting the South Pacific subtropical circulation: A synthesis of World Ocean Circulation Experiment observations along 32°S, *J. Geophys. Res.*, *106*, 19,481–19,513.

M. J. Follows, Program in Atmospheres, Oceans and Climate, Department of Earth, Atmosphere and Planetary Sciences, Massachusetts Institute of Technology, 77 Massachusetts Avenue, Cambridge, MA 02139, USA. (mick@plume.mit.edu)

R. M. Key, Atmospheric and Oceanic Sciences Program, Princeton University, Princeton, NJ 08544, USA. (key@geo.princeton.edu)

V. Roussenov and R. G. Williams, Department of Earth and Ocean Sciences, University of Liverpool, Liverpool L69 3GP, UK. (ric@liverpool.ac.uk)